

## Effect of Freestream Turbulence on Flow Separation Around Ahmed Body

**Amir Sagharichi**

Department of Mechanical Engineering  
University of Manitoba  
Winnipeg, Manitoba, R3T 5V6, Canada  
Sagharia@myumanitoba.ca

**Mark F. Tachie**

Department of Mechanical Engineering  
University of Manitoba  
Winnipeg, Manitoba, R3T 5V6, Canada  
mark.tachie@umanitoba.ca

### ABSTRACT

This study investigates the effects of freestream turbulence (FST) on the spatiotemporal flow characteristics around a slanted-back Ahmed body with a square leading edge using the time-resolved particle image velocimetry (TR-PIV). The Reynolds number based on the freestream velocity and body height is  $Re_H = 1.7 \times 10^4$ . Two passive grids are deployed at the inlet of the water channel to elevate the FST intensity to 5.0% and 15.0%, and the results are compared to those obtained at an FST intensity of 1.5% (without grid). Mean velocity, two-point auto-correlation, and Reynolds normal stresses are employed to analyze flow structures around the body, while proper orthogonal decomposition (POD) is used to study the effect of FST on coherent structures and associated frequencies. The results indicate a monotonic reduction in the size of the recirculation bubble over the roof with increasing FST intensity, but significant change is observed in the wake region. The peak value of streamwise Reynolds normal stress over the roof increases with FST. In contrast, the peak value of vertical Reynolds normal stress around the body is independent of FST intensity. FST intensity also enhances the spatial correlation of streamwise fluctuation velocities over the roof, with no discernible trend in the wake region. Over the roof, coherent structures and their associated frequencies show no significant difference for the two lower FST levels. However, increasing FST intensity decreases the dominant frequency in the wake region.

### INTRODUCTION

The transportation industry, especially on-road vehicles, continues to play a significant role in worldwide energy consumption and the release of pollutants. As a result, manufacturers are now obligated to adhere to ever-tightening environmental guidelines, including stringent CO<sub>2</sub> emissions standards (Burton et al., 2021). A promising strategy to comply with these regulations involves reducing aerodynamic drag through the implementation of innovative flow control techniques. Due to the intimate relationship between the dynamics of separated flow and aerodynamic drag around on-road vehicles (Joseph et al., 2012), a comprehensive understanding of the unsteady flow dynamics is required for the development of these drag reduction techniques.

Ahmed body is a simplified model that has been widely used by researchers to simulate the flow structure around full-scale on-road vehicles (Zhang et al., 2015; Wang et al., 2020; Sagharichi et al., 2023). Previous research on the slanted-back Ahmed body showed that the flow topology consists of separated shear layers emanating from both the leading and upper edges of the slanted surface, longitudinal C-pillar vortices near each side edge of the slanted surface, and a pair of recirculation regions (toroidal structure) behind the vertical base (Zhang et al., 2015).

Most of the previous studies that examined the flow structures around Ahmed bodies were conducted at FST intensities ( $T_u = u_{rms}/U_\infty$ , where  $u_{rms} = \sqrt{\overline{u'^2}}$  is root-mean-square of the streamwise fluctuation velocity  $u'$ ,  $(\bar{\cdot})$  denotes time

averaging, and  $U_\infty$  is freestream velocity) of less than  $T_u = 2\%$  (Sagharichi et al., 2023). However, real-world scenarios often entail incoming flows characterized by higher levels of FST. According to Wordley and Saunders (2008), FST intensity in open-road conditions can vary from  $T_u = 2\%$  to 16%, the latter being an order of value higher than the typical FST conditions examined in experimental settings. This underscores the necessity for refined experiments at elevated FST levels to understand their impacts on the flow structures around on-road vehicles.

Recently, there has been an interest in studying the impact of FST level on the flow dynamics around the square-back Ahmed body, and these studies have provided valuable insights into how FST affects aerodynamic performance. Aleyasin et al. (2021) investigated the impact of FST intensity on the wake dynamics around two elongated bluff bodies, including a square-back Ahmed body. By varying FST intensity ( $T_u = 4\%$  and  $T_u = 7\%$ ), it was observed that the peak value of streamwise Reynolds normal stress ( $\overline{u'u'}$ ) increased by 70% and two dominant frequencies  $St$  ( $fH/U_\infty$ , where  $f$  and  $H$  are vortex shedding frequency and body height, respectively) = 0.360 and 0.280 were identified in the wake region at  $T_u = 7\%$  compared to a dominant frequency of  $St = 0.163$  at  $T_u = 4\%$ . The authors also reported a 25% increase in the reverse flow area in the wake region with increased FST intensity. This observation is at variance with Passaggia et al. (2021) who observed that increasing FST intensity and integral length scale ( $L_u$ , which represents the typical size of the largest eddies) led to a decrease in wake recirculation length. Additionally, higher FST levels were correlated with a reduced pressure gradient behind the base, resulting in 18% drag reduction in the highest FST level ( $T_u = 12.9\%$  and  $L_u = 0.60H$ ) compared to the lowest level ( $T_u = 0.5\%$  and  $L_u = 0.22H$ ). These observations are also at variance with those made by Wang et al. (2020) who reported that base pressure remains unchanged with increasing FST intensity. The study of Burton et al. (2021) focused on the influence of FST on the wake bistability phenomenon in the wake region. They varied FST intensity levels from  $T_u = 1\%$  to 16% by deploying horizontal slats and grids at the wind tunnel inlet. Analysis of base-pressure measurements revealed bistability in the lateral direction for both high and low turbulence levels, with the switching rate between positive and negative values of  $\partial C_p / \partial y$  (lateral base-pressure gradient) increasing with FST intensity. This behavior is inconsistent with the earlier observation of Cadot et al. (2020) who reported that the switching rate decreases under the higher FST intensity. The only study on the effect of FST intensity on slanted back Ahmed body focused on the vortex shedding frequency of separation bubbles. Zhang et al. (2015) introduced a passive regular grid upstream which increased the FST intensity from  $T_u = 0.3\%$  (background FST intensity) to  $T_u = 7.8\%$ . At the higher FST intensity, no dominant spectral peak was observed near the leading surface of the body but two distinct peaks at  $St = 0.12$  and 0.17 were identified at the lower FST due to pulsation of the recirculation

bubbles near the leading edge at the lower FST level. Nonetheless, the vortex shedding frequency in the wake region remained unchanged ( $St = 0.37$ ) regardless of the level of the FST intensity.

In this study, TR-PIV is used to evaluate the effects of FST on the spatiotemporal dynamics of the separated flow around a slanted-back Ahmed body with a square leading edge. Two elevated FST levels ( $T_u = 5.0\%$  and  $15.0\%$ ) were generated using passive grids placed upstream of the Ahmed body and the results are compared with a baseline test case (i.e. without grids installed upstream of the Ahmed body) with a lower FST level of  $T_u = 1.5\%$ .

## EXPERIMENTAL METHOD

### Experimental Set-up

The experiments were carried out in an open recirculating water channel in the Turbulence and Hydraulic Engineering Laboratory (THEL) at the University of Manitoba. The streamwise length, spanwise width, and vertical height of the test section are 6000 mm, 600 mm, and 450 mm, respectively. The test section was fabricated from 31.8 mm thick Super Abrasion Resistant transparent acrylic plates to facilitate optical access. The water depth was set to 435 mm height.

A 1:4 model of the full-scale square leading-edge Ahmed body with a rear slant angle of  $\alpha = 25^\circ$  was used. Figure 1 shows a schematic representation of the body, and the adopted Cartesian coordinate system. The model has an overall length of  $L = 261$  mm, width of  $B = 97$  mm, and height of  $H = 72$  mm, supported by four cylindrical struts of  $C = 12.50$  mm height and  $d = 7.50$  mm diameter.

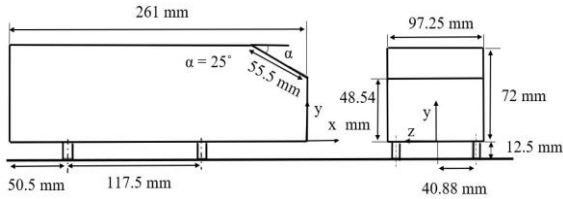


Figure 1. Schematic of Ahmed body

The body was installed on a raised plate with a length of  $42H$  that spanned the entire width of the test section and installed horizontally 50 mm above the floor to control the growth of the boundary layer. The blockage ratio (the ratio between the body frontal area and the rectangular cross-stream area of the water column above the raised floor) was 3%. The leading edge of the body was positioned 200 mm downstream from the leading edge of the plate.

The freestream velocity was set to  $U_\infty = 0.24$  (m/s) which led to the Reynolds number based on the body height of  $Re_H = U_\infty H / \nu = 1.7 \times 10^4$ , where  $\nu$  is the kinematic viscosity of water at  $T = 20^\circ\text{C}$ . The FST intensity measured along the centerline of the channel was  $T_u = 1.5\%$ . Throughout this paper, parameters are normalized relative to the model height and freestream velocity, using the following notations:  $x^* = x/H$ ,  $y^* = y/H$ , and  $U^* = U/U_\infty$ .

### Turbulence Generation

To produce elevated FST intensity levels, two passive grids: a fractal grid, denoted as F41, and a regular grid, denoted as R48 were fabricated from stainless steel and installed at the inlet of the test section. These grids have blockage ratios of  $\sigma = 41\%$  and  $48\%$ , respectively. Schematics of the grids and their geometric

specifications are depicted in Figure 2 and Table 1, respectively. In Table 1,  $N$  represents iterations of the fractal patterns,  $L_0$  is the maximum bar length in F41 (the bar length in the R48), and  $t_0$  is the spanwise thickness of the largest bar in F41 (the bar thickness of R48), and  $t_r$  represents thickness ratio (ratio of the largest bar to the thinnest bar).

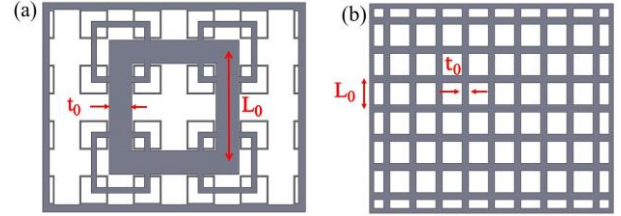


Figure 2. Turbulence-generating grids. (a) F41, (b) R48

Table 1. Grids specifications

Parameters	F41	R48
$N$	3	-
$L_0/H$	3.30	0.87
$t_0/H$	0.70	0.21
$t_r$	17	1
$\sigma \%$	41	48

The F41 and R48 grids were positioned at distances of 350 mm and 160 mm, respectively, downstream of the test section inlet. Care was taken to ensure that the leading edge of the body was placed in the decay region of the grids where the turbulence is approximately homogeneous and isotropic (Hurst and Vassilicos, 2007). Following the installation of the grids, the FST intensity at the location of the leading edge increased to  $T_u = 5.0\%$  for R48 and  $T_u = 15.0\%$  for F41. Further details are given in Table 2, where  $x$ ,  $x_{GL}$  and  $x_{LL}$  are the distance from the grid to the body leading edge, distance from the grid to the raised plate leading edge, and distance from the raised plate leading edge to the body leading edge, respectively.

Table 2. Details of the experimental setup

Grid	$u_{rms}/v_{rms}$	$T_u$ (%)	$L_u/H$	$x$ (mm)	$x_{GL}$ (mm)	$x_{LL}$ (mm)
-	1.05	1.5	-	-	-	2.77
R48	1.13	5.0	0.68	21.95	19.16	2.77
F41	1.14	15.0	1.0	19.30	16.52	2.77

### Data Acquisition

Time-resolved particle image velocimetry was used to measure the velocity vectors in the  $x$ - $y$  plane, at the midspan of the test section. The flow was seeded with silver-coated hollow glass spheres of diameter  $10 \mu\text{m}$  and a specific gravity of  $\rho_p = 1.4$ . Flow field illumination was provided by a dual-cavity, dual-head high-speed Neodymium-doped yttrium lithium fluoride (Nd: YLF) laser. Two high-speed CMOS cameras with a resolution of  $2560 \text{ pixel} \times 1600 \text{ pixel}$  were used to capture the particle images. The PIV field of view (FOV) for each camera was  $4H \times 2.50H$  with an image magnification of  $112.5 \mu\text{m}/\text{pixel}$ . 60 000 images were collected at a sampling frequency of 803 Hz to resolve all dynamically important vortical structures. A schematic of the PIV setup is provided in Figure 3.

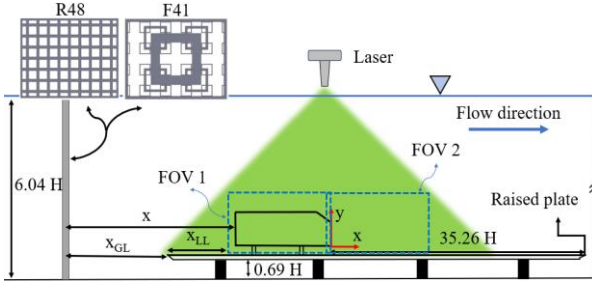


Figure 3. Schematic of the experimental setup

The images were post-processed using commercial software (Davis version 10.2.1) supplied by LaVision Inc. Vector fields were computed using a GPU-accelerated multi-pass cross-correlation algorithm with an initial interrogation window of 128 pixels  $\times$  128 pixels with 50 % overlap followed by final four passes with an interrogation window of 24 pixel  $\times$  24 pixel and 75% overlap, leading to the spatial resolution of 0.037H.

## RESULTS AND DISCUSSION

### Time-averaged flow field

Figure 4 depicts the contour of streamwise ( $U^*$ ) and vertical ( $V^*$ ) mean velocities around the Ahmed body exposed to different FST intensities, with mean streamlines overlaid. The solid red line represents the isopleth of  $U^* = 0$ , which defines the recirculation region. The plots illustrate the formation of a recirculation region encompassing the low-velocity region over the roof and the wake region with respective streamwise lengths of  $L_{rr}^*$  and  $L_{rw}^*$ . There is a monotonic decrease in the size of the recirculation region over the roof with FST level. Specifically, the recirculation length decreases from  $L_{rr}^* = 1.85$  for  $T_u = 1.5\%$  to  $L_{rr}^* = 0.84$  for  $T_u = 15.0\%$ , representing a 55% reduction. A decrease in recirculation length was also observed over the rectangular cylinder subjected to elevated FST levels (Kiyama and Sasaki, 1983) and was attributed to the earlier recovery of surface pressure due to higher entrainment of flow into the recirculation region. In the wake region, two recirculation bubbles in the shape of a toroidal structure are formed due to the interaction of shear layers emanating from the slanted surface and under the base, with  $L_{rw}^* \approx 0.53$  regardless of FST level. Contours of vertical mean velocity show clusters of upwash ( $V^* > 0$ ) and downwash ( $V^* < 0$ ) flow in the vicinity of the leading edge and slanted surface of the body. While there is a 13.2% increase in maximum upwash velocity near the leading edge with an increase in FST intensity to  $T_u = 5.0\%$ , it reduces with a further increase to  $T_u = 15.0\%$ . Nonetheless, the maximum downwash flow remains nearly independent of the FST intensity level.

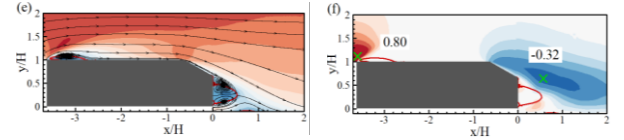
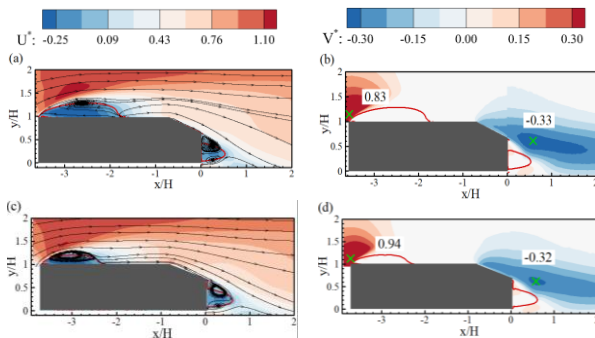


Figure 4. Streamwise (left column) and vertical (right column) mean velocity contours for  $T_u = 1.5\%$  [(a), (b)];  $T_u = 5.0\%$  [(c), (d)] and  $T_u = 15.0\%$  [(e), (f)]

The contours of streamwise ( $\overline{u'u'}$ ) and vertical ( $\overline{v'v'}$ ) Reynolds normal stresses are presented in Figure 5. The peak value of each quantity and their locations are indicated in the figure. The figure shows that the locations of the peak values of  $\overline{u'u'}$  and  $\overline{v'v'}$  shift upstream and closer to the roof with increasing FST intensity, consistent with the shortening of the recirculation region near the leading edge (Figure 4). This behavior can be attributed to the enhanced turbulent entrainment and mixing with increasing FST levels. Also, a peak value of  $\overline{u'u'} = 0.14$  is observed in the shear layer emanating from the body leading edge subjected to  $T_u = 1.5\%$ , which is 14% and 78% lower than those in  $T_u = 5.0\%$  and  $T_u = 15.0\%$ , respectively. The increase in  $\overline{u'u'}$  with increasing FST level is consistent with the observations made by Aleyasin et al. (2021). Similarly, the peak value of  $\overline{v'v'}$  increases from 0.05 to 0.06 as FST intensity increases from  $T_u = 1.5\%$  to 5.0%, but no further increase is observed when the FST intensity is increased from  $T_u = 5.0\%$  to 15.0%. However, varying FST intensity of the approaching flow has no significant effect on the peak value of the Reynolds stresses in the wake region.

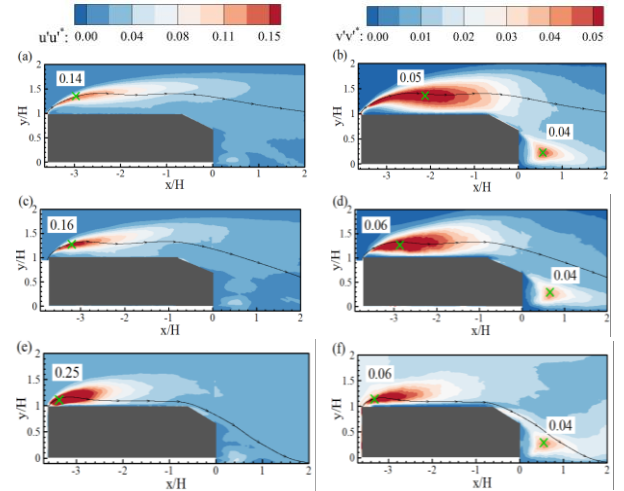


Figure 5. Streamwise (left column) and vertical (right column) Reynolds normal stress for  $T_u = 1.5\%$  [(a), (b)];  $T_u = 5.0\%$  [(c), (d)] and  $T_u = 15.0\%$  [(e), (f)]. The mean streamline emanating from the leading edge has been superimposed.

### Two-point auto-correlation

The influence of the FST intensity on spatial correlation around the body is investigated using the spatial two-point auto-correlation of streamwise velocity fluctuation, which is defined as follows:

$$R_{uu}(x^*, y^*, x_{ref}^*, y_{ref}^*) = \frac{\overline{u'(x_{ref}^*, y_{ref}^*)u'(x^*, y^*)}}{u_{rms}(x_{ref}^*, y_{ref}^*)u_{rms}(x^*, y^*)} \quad (1)$$

In Equation 1,  $(x_{ref}^*, y_{ref}^*)$  is the reference point. The reference points are chosen at the locations of maximum  $\overline{u'u'}$  within the

shear layer emanating from the leading edge,  $(x_{ref}^*, y_{ref}^*) = (-0.64, 1.10)$  over the slanted surface, and at the maximum  $\overline{v'v'}$  in the wake region. In this analysis,  $x' = x^* - x_{ref}^*$  and  $y' = y^* - y_{ref}^*$ . Figure 6 displays the contours of  $R_{uu}$  for the different FST intensities. The contours range from 0.4 to 1, increasing by increments of 0.1. Near the leading edge and on the slanted surface, the spatial correlation in both the  $x$  and  $y$  directions significantly increases with increasing FST intensity level. However, no systematic trend with FST is observed in the wake region. This behavior further highlights the lack of sensitivity of the streamwise Reynolds normal stresses to the FST intensity level in the wake region (Figure 5).

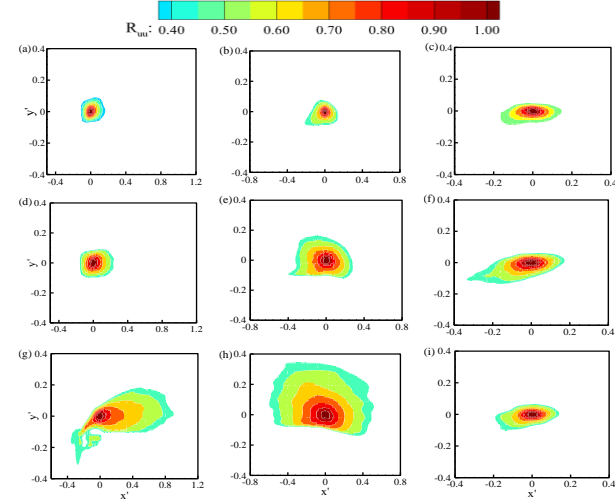


Figure 6. Two-point auto-correlation of the streamwise fluctuation velocity near the leading edge (left column), over the slanted surface (middle column), and in the wake region (right column) for  $T_u = 1.5\%$  [(a), (b) and (c)];  $T_u = 5.0\%$  [(d), (e) and (f)] and  $T_u = 15.0\%$  [(g), (h) and (i)]

The longitudinal integral length scale is determined by integrating the spatial two-point auto-correlation function of streamwise fluctuation velocity (Equation 2).

$$L_u(x^*, y^*) = \int_0^{x'_0} R_{uu}(x^*, y^*, x_{ref}^*, y_{ref}^*) dx' \quad (2)$$

where  $x'_0$  is the first zero crossing. Table 3 shows the integral length scales corresponding to the spatial auto-correlations shown in Figure 6. It is evident that increasing FST intensity increases the integral length scale over the roof and slanted surface. Notably, as FST intensity rises to  $T_u = 5.0\%$ , the integral length scale nearly doubles near the leading edge and slanted surface, and triples when FST intensity increases from  $T_u = 5\%$  to  $15.0\%$ . However, FST has no significant effects on turbulence length scale in the wake region. These results align with the findings of Chen et al. (2022).

Table 3. Longitudinal integral length scale around the body

$T_u$	Leading edge	Slanted surface	Wake region
1.5%	0.15H	0.15H	0.15H
5.0%	0.31H	0.36H	0.15H
15.0%	1.01H	1.15H	0.19H

### Proper orthogonal decomposition

To assess how FST intensity influences the most energetic structures and their associated frequencies around the body, proper orthogonal decomposition (POD) is employed. The POD algorithm was performed using the snapshot technique introduced by Sirovich (1987) and detailed in Fang and Tachie (2019a). To isolate the effect of FST intensity on the energetic structures and their associated frequencies over the roof and in the wake region, the POD analysis was performed separately over the roof ( $x^* \in [-3.80, 0]$  and  $y^* \in [1.0, 2.22]$ ) and in the wake region ( $x^* \in [0, 3.80]$  and  $y^* \in [-0.17, 1.0]$ ). Figure 7 illustrates the relative turbulence kinetic energy (TKE) captured by the first 100 modes over the roof (Figure 7(a)) and wake region (Figure 7(b)) at different FST intensity levels. The plots show that, except for  $T_u = 15.0\%$ , the first two modes approximately capture similar levels of TKE. Over the roof, the first (or second) mode for  $T_u = 1.5\%$  and  $5.0\%$  captures 9% and 7%, respectively, of the total TKE. However, when  $T_u = 15.0\%$ , the first mode captures 14%, which is twice the energy captured by the second mode. In the wake region, no significant disparity is observed in the modal energy distribution at two lower FST intensities. At these FST levels, each of the first two modes captures approximately 5% of TKE. Elevating FST intensity to  $T_u = 15.0\%$  increases the energy of the first mode to 13% compared to 5% for the second mode.

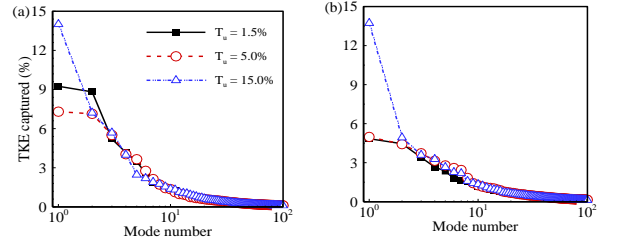


Figure 7. Relative TKE captured by POD modes. (a) over the roof and (b) in the wake region.

Figure 8 examines the spatial dynamics of the first and second POD modes using vertical fluctuating velocity ( $v'$ ) over the roof.

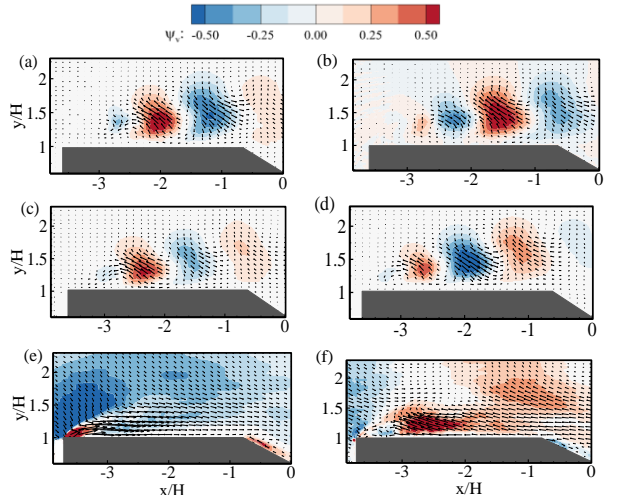


Figure 8. Contours of the first [(a), (c), and (e)] and second [(b), (d), and (f)] POD modes superimposed by the corresponding vector field over the roof.  $T_u = 1.5\%$  [(a), (b)];  $T_u = 5.0\%$  [(c), (d)] and  $T_u = 15.0\%$  [(e), (f)].

The roof of the body subjected to  $T_u = 1.5\%$  (Figures 8(a) and 8(b)) is characterized by alternate positive and negative

structures that emanate from the leading edge. Similar alternate structures are observed over the body exposed to  $T_u = 5.0\%$  (Figures 8(c) and 8(d)) except for the center of negative and positive structures which is positioned closer to the leading edge of the body at  $T_u = 5.0\%$ . Specifically, for the first mode, the center of the first two structures occurs at  $x/H = -2.05$  and  $-1.05$  for  $T_u = 1.5\%$ , while it occurs at  $x/H = -2.37$  for  $-1.37$  for  $T_u = 5.0\%$ . Comparing the spatial patterns of the first and second modes for  $T_u = 1.5\%$  and  $T_u = 5.0$  shows that their topology is similar but shifted by one-quarter wavelength. Following Thacker et al. (2013) the distance between the peaks of successive positive and negative structures in the first paired mode represents half of the wavelength ( $\lambda/2$ ) of the most energetic structures in turbulent flow. This value over the roof for both  $T_u = 1.5\%$  and  $T_u = 5.0\%$  is  $\lambda/2 = 1.02H$ . The spatial structure of the first two POD modes for  $T_u = 15.0\%$  (Figures 8(e) and 8(f)) is significantly different from those observed for  $T_u = 1.5\%$  and  $T_u = 5.0\%$ . While the spatial structure of the first mode (Figure 8(e)) is characterized by a large negative and small positive structure in the vicinity of the leading edge, the energetic structures in the second mode (Figure 8(f)) are concentrated near the end of the recirculation region.

Figure 9 illustrates the spatial distributions of the first and second POD modes in the wake region. Similar to the roof region, the wake region of the  $T_u = 1.5\%$  and  $5.0\%$  cases (Figures 9(a) to 9(d)) are characterized by alternate shedding of vortices, indicated by a succession of positive and negative fluctuations. Similar alternating regions of positive and negative structures have been reported in the wake region of slanted-back Ahmed bodies (Siddiqui and Agelin-Chaab, 2022). The positive and negative structures in the first and second modes of  $T_u = 1.5\%$  and  $T_u = 5.0\%$  are characterized by a shift of one-quarter wavelength. Considering the comparable relative TKE captured by these two modes (Figure 7(b)) it can be inferred that the mode pairing also exists in the wake region of  $T_u = 1.5\%$  and  $T_u = 5.0\%$ , with respective  $\lambda/2 = 0.68H$  and  $0.78H$ . While no evidence of alternate vortex shedding is observed in the wake region of the  $T_u = 15.0\%$  in the first mode (Figure 9(e)), the second mode is characterized by positive and negative structures that emanate from the undersurface of the body and expand as it evolves downstream (Figure 9(f)).

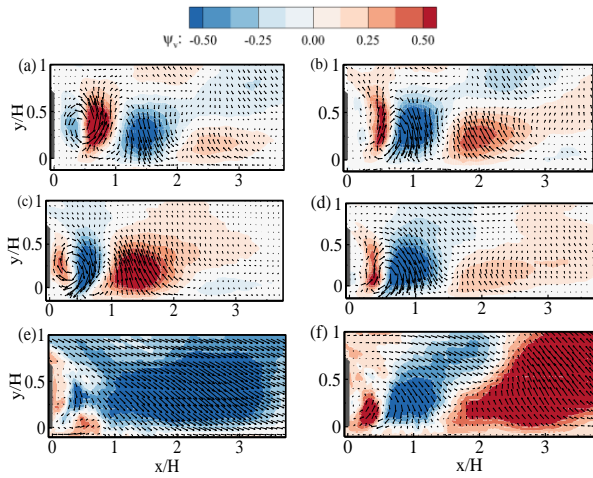


Figure 9. Contours of the first [(a), (c), and (e)] and second [(b), (d), and (f)] POD modes superimposed by the corresponding vector field in the wake region.  $T_u = 1.5\%$  [(a), (b)];  $T_u = 5.0\%$  [(c), (d)] and  $T_u = 15.0\%$  [(e), (f)].

Figure 10 shows the pre-multiplied frequency spectra of the temporal coefficients corresponding to the first two POD modes. The plots show a similar dominant frequency of  $St = 0.36$  over the roof for the two lower FST levels (Figures 10(a) and 10(c)). This frequency is consistent with  $St = 0.37$  observed over a cuboid subjected to FST intensity of  $T_u = 4.0\%$  (Aleyasin et al., 2021). The presence of a unique dominant frequency over the roof for  $T_u = 1.5\%$  and  $5.0\%$  shows that these FST levels are not intense enough to suppress the separated shear layers over the body. In contrast, a significantly lower frequency of  $St = 0.07$  and its harmonics ( $St = 0.14$  and  $0.23$ ) are observable for the first POD mode over the body exposed to  $T_u = 15.0\%$  (Figures 10(e)). A similar low frequency was observed by Simoni et al. (2017) and Fang and Tachie (2019b) in their POD analysis at elevated FST levels. The spectrum of the second mode is significantly different from the first mode and is characterized by low-energy dual peaks at  $St = 0.14$  and  $0.23$ . In the wake region, the frequency of the first two POD modes for  $T_u = 1.5\%$  is  $St = 0.23$  (Figure 10(b)) but decreases to  $St = 0.19$  for  $T_u = 5.0\%$  (Figure 10(d)). For FST intensity of  $T_u = 15.0\%$  (Figure 10(f)), the dominant frequency and its harmonic for the first mode ( $St = 0.07$  and  $0.14$ ) resemble that observed for the first mode over the roof. Meanwhile, the second mode is characterized by a dominant frequency of  $St = 0.19$  and its harmonic,  $St = 0.38$ . The presence (absence) of the fundamental frequency in the second (first) mode indicates that increasing the FST intensity to  $T_u = 15.0\%$  shifts the mode associated with alternate positive and negative structures from mode one to the second mode.

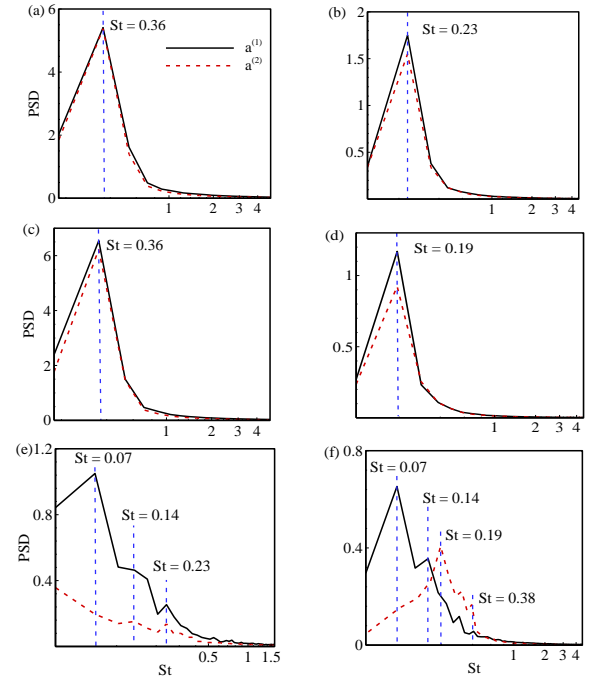


Figure 10. Frequency spectra of the POD time coefficients over the roof [(a), (c), and (e)] and wake region [(b), (d), and (f)].  $T_u = 1.5\%$  [(a), (b)];  $T_u = 5.0\%$  [(c), (d)] and  $T_u = 15.0\%$  [(e), (f)].

## CONCLUSION

The present study investigated the impact of FST intensity on the flow characteristics around a squared-leading edge Ahmed body. Two passive grids were employed to increase FST intensity to  $T_u = 5.0\%$  and  $15.0\%$  and the results were compared with those of  $T_u = 1.5\%$ . The results demonstrate that higher FST levels lead to a reduction in the recirculation length

over the roof. Additionally, there was an increase in the maximum upwash velocity near the leading edge as FST intensity increased to  $T_u = 5.0\%$ , however, beyond this threshold, the maximum upwash velocity is reduced. Increasing the FST level did not change the recirculation length and the downwash flow distribution in the wake region. The peak value of the streamwise Reynolds normal stress over the roof increased monotonically with increasing FST intensity, but no significant change was observed in the peak value of the vertical Reynolds normal stress. The peak value of Reynolds normal stresses in the wake region were independent of FST intensity. Higher FST level also increased the longitudinal integral length scale over the roof, but no systematic effect was observed in the wake region. POD analysis of the first and second modes showed alternative positive and negative structures over the roof and wake region of the body subjected to  $T_u = 1.50\%$  and  $T_u = 5.0\%$ . Increasing the FST intensity from  $T_u = 1.5\%$  to  $T_u = 5.0\%$  did not alter the dominant frequency ( $St = 0.36$ ) of the first and second POD modes over the roof but it led to a decrease in frequency from  $St = 0.23$  to  $0.19$  in the wake region. Further increasing the FST intensity to  $T_u = 15.0\%$  resulted in a substantial change in the POD distribution, marked by a low frequency of  $St = 0.07$  over the roof and wake region for the first POD mode while the spatial structure of the second POD mode in the wake region was characterized by alternate positive and negative structures with the dominant frequency of  $St = 0.19$ .

#### ACKNOWLEDGMENTS

The authors express their gratitude for the financial support provided by the Natural Sciences and Engineering Research Council of Canada (NSERC) to M.F.T. Additionally, they acknowledge the Canada Foundation for Innovation (CFI) for funding the experimental facility used in this work.

#### REFERENCES

- Aleyasin, S.S., Tachie, M.F. and Balachandar, R., 2021. "Characteristics of flow past elongated bluff bodies with underbody gaps due to varying inflow turbulence", *Physics of Fluids*, Vol. 33.
- Burton, D., Wang, D., Smith, T., Scott, H. N., Crouch, T. N., and Thompson, M. C., 2021, "The influence of background turbulence on Ahmed-body wake bistability", *Journal of Fluid Mechanics*, Vol. 926.
- Cadot, O., Almarzooqi, M., Legeai, A., Parezanović, V. and Pastur, L., 2020, "On three-dimensional bluff body wake symmetry breaking with free-stream turbulence and residual asymmetry", *Comptes Rendus. Mécanique*, Vol. 348, pp. 509-517.
- Chen, Y., Djidjeli, K. and Xie, Z.T., 2022, "Freestream turbulence effects on the aerodynamics of an oscillating square cylinder at the resonant frequency", *Fluids*, Vol. 7, p.329.
- Fang, X. and Tachie, M.F., 2019a, "On the unsteady characteristics of turbulent separations over a forward-backward-facing step", *Journal of Fluid Mechanics*, Vol. 863, pp. 994-1030.
- Fang, X. and Tachie, M.F., 2019b, "Flows over surface-mounted bluff bodies with different spanwise widths submerged in a deep turbulent boundary layer", *Journal of Fluid Mechanics*, Vol. 877, pp.717-758.
- Hurst, D. and Vassilicos, J.C., 2007. "Scalings and decay of fractal-generated turbulence", *Physics of Fluids*, Vol. 19.
- Joseph, P., Amandolese, X., and Aider, J., 2012, "Drag reduction on the 25° slant angle Ahmed reference body using pulsed jets", *Experiments in Fluids*, Vol. 52, pp. 1169–1185.
- Kiya, M. and Sasaki, K., 1983. "Free-stream turbulence effects on a separation bubble", *Journal of Wind Engineering and Industrial Aerodynamics*, Vol. 14, pp. 375-386.
- Passaggia, P. Y., Mazellier, N., and Kourta, A., 2021, "Aerodynamic drag modification induced by free-stream turbulence effects on a simplified road vehicle", *Physics of Fluids*, Vol. 33, pp. 105-108.
- Sagharichi, A., Aleyasin, S. S., and Tachie M. F., 2023, "Turbulent separations around a slanted-back Ahmed body with square and rounded leading edge", *Physics of Fluids*, Vol. 4, pp. 045129.
- Siddiqui, N.A. and Agelin-Chaab, M., 2022, "Experimental investigation of the flow features around an elliptical Ahmed body", *Physics of Fluids*, Vol. 34.
- Simoni, D., Lengani, D., Ubaldi, M., Zunino, P. and Dellacasagrande, M., 2017, "Inspection of the dynamic properties of laminar separation bubbles: free-stream turbulence intensity effects for different Reynolds numbers", *Experiments in Fluids*, Vol. 58, pp.1-14.
- Sirovich, L., 1987, "Turbulence and the dynamics of coherent structures. I. Coherent structures", *Quarterly of Applied Mathematics*, Vol. 45, pp. 561-571.
- Thacker, A., Aubrun, S., Leroy, A. and Devinant, P., 2013. "Experimental characterization of flow unsteadiness in the centerline plane of an Ahmed body rear slant", *Experiments in fluids*, Vol. 54, pp. 1-16.
- Wang, S., Scott, H., Crouch, T., Thompson, M., and Burton, T., 2020, "The Effects of Free Stream Turbulence on Bistability of the Ahmed Body Wake" *22nd Australasian Fluid Mechanics Conference AFMC2020 Brisbane*, Australia.
- Wordley, S. and Saunders, J., 2008, "On-road turbulence", *SAE International Journal of Passenger Cars-Mechanical Systems*, Vol. 1, pp. 341-360.
- Zhang, B. F., Zhou, Y., and To S., 2015, "Unsteady flow structures around a high-drag Ahmed body", *Journal of Fluid Mechanics*, Vol. 777, pp. 291-326.